Extrusion dynamics of deep-water volcanoes on stretched continental crust

Qiliang Sun[1,2,3], Christopher A-L. Jackson[4], Craig Magee[4,5], Samuel J. Mitchell[6] and Xinong Xie[1,3]

[1]Key Laboratory of Tectonics and Petroleum Resources, China University of Geosciences (Wuhan), Ministry of Education, Wuhan 430074, China;

[2]Laboratory for Marine Mineral Resources, Qingdao National Laboratory for Marine Science and Technology, Qingdao 266061, China;

[3]College of Marine Science and Technology, China University of Geosciences (Wuhan), Wuhan, Hubei 430074, PR China;

[4]Basins Research Group (BRG), Department of Earth Science &Engineering, Imperial College, London, SW7 2BP, UK

[5]School of Earth and Environment, University of Leeds, Leeds, LS2 9JT, UK

[6]Department of Earth Sciences, University of Hawai'i at Mānoa, 1680 East West Road, Honolulu, HI 96822, USA

Abstract

Submarine volcanism accounts for c. 75% of the Earth's volcanic activity. However, difficulties with imaging their exteriors and interiors mean deep-water volcanoes remain poorly understood in terms of their extrusion dynamics and erupted volume. Here, we use high-resolution 3-D seismic reflection data to examine the geometry, distribution, and extrusion dynamics of two Late Miocene-Quaternary, well-imaged, deep-water (>2.0 km emplacement depth) volcanoes in the

South China Sea buried beneath ~55-330 m of sedimentary strata. The volcanoes, which have crater-like basal contacts that truncate underlying strata, erupted lava flows feeding lobate lava fans. The lava flows are >9 km and contain lava tubes that have rugged basal contacts defined by ~90±23 m high erosional ramps. We suggest the lava flows eroded down into and were emplaced at shallow depths within wet, unconsolidated, near-seafloor sediments. Extrusion dynamics were likely controlled by low magma viscosities, high hydrostatic pressures, and soft, near-seabed sediments, which collectively are characteristic of deep-water environments. Because the lava flows and volcanic edifices are imaged in 3D, we calculate the lava flows account for 50–97% of the total erupted volume. Our results indicate deep-water volcanic edifices may form a minor component of the extrusive system, and that accurate estimates of erupted volume requires knowledge of the basal surface of genetically related lava flows. We conclude that 3D seismic reflection data is a powerful tool for constraining the geometry and extrusion dynamics of buried, deep-water volcanic features; such data should be used to image and quantify extrusion dynamics of modern deep-water volcanoes.

Keywords

Volcano, deep-water, lava flow, seismic reflection, South China Sea

1. Introduction

The external morphology of volcanoes and their eruptive products reflect, and provide insights into, the processes controlling magma extrusion and volcano construction (e.g. Walker, 1993; Planke et al., 2000; Grosse and Kervyn, 2018). By extracting high-resolution, quantitative data on the morphology of modern and, in some cases, still active volcanic edifices and surrounding lava flows from airborne/shuttle radar topography or time-lapse multi-beam bathymetry, we can estimate erupted volume and reconstruct volcano growth mechanisms (e.g. Holcomb et al., 1988; Walker, 1993; Goto and McPhie, 2004; Cocchi et al., 2016; Somoza et al., 2017; Allen et al., 2018; Grosse and Kervyn, 2018). Whilst remote sensing data capture the external morphology of volcanoes and lava flows, they do not image their basal surface or internal architecture. Without access to the full 3D structure of these extrusive systems, it is difficult to assess the accuracy of estimated volumes of erupted material, or test volcano growth and lava emplacement models.

Several studies demonstrate that seismic reflection data can be used to map the external morphology and internal architecture of buried volcanoes in 3D (e.g. Planke et al., 2000; Calvès et al., 2011; Jackson, 2012; Magee et al., 2013; Reynolds et al., 2017). To-date, most studies have focused on volcanoes formed in sub-aerial or shallow-marine environments (e.g. Planke et al., 2000; Jackson, 2012; Magee et al., 2013; Reynolds et al., 2018), although seismic reflection surveys have been used to image the shallowly buried flanks of deep-water volcanoes (e.g. Funck et al. 1996). The 3D geometry, internal structure, extrusion dynamics, and volume of deep-water volcanoes located along the rifted margins, thus, remain poorly documented.

We use high-resolution 3D seismic reflection data to examine two, Late Miocene-Quaternary submarine volcanoes that were emplaced in deep-water (>2.0 km) on highly stretched continental crust in the northern South China Sea, and that are now buried by a ~55-330 m thick sedimentary succession (Fig. 1). By interpreting volcano and lava flow structure, distribution, and scale, we determine emplacement processes, calculate erupted volume distributions, and relate our findings to studies of deep-water volcanoes that use bathymetry and remote sensing data. In particular, we show basal surfaces of volcanic edifices and lava flows are rugged, with 50–97% of the total erupted material hosted within the latter; i.e. the volcano edifices only comprise only a small portion of the total erupted magma volume. Our observations suggest erupted volumes calculated from airborne/shuttle radar topography or time-lapse multi-beam bathymetry data, which typically assume a smooth base to imaged volcanoes and lava flows, may be severely underestimated. We conclude the high hydrostatic pressure of the deep-water environment controlled erupting lava rheology and, consequently, volcano and lava flow morphology.

2. Geological setting

The study area is located in the Pearl River Mouth Basin, on the northern, highly stretched continental crust of the South China Sea (Franke, 2013; Zhao et al., 2016) (Fig. 1a). The South China Sea was an area of subduction in the late Mesozoic, before the onset of continental rifting and subsequent seafloor spreading in the Cenozoic (e.g. Taylor and Hayes, 1983; Briais et al., 1993; Franke et al., 2014; Li et al., 2014; Sun et al., 2014a; Ding and Li, 2016). A lack of seaward-dipping reflections (SDRs), and low volumes of rift-related igneous rocks, suggest the northern part of the South China Sea is a magma-poor margin (Cameselle et al., 2017; Yan et al., 2006; Franke, 2013). Seafloor spreading ceased at ~15 Ma (Li et al., 2014), with post-rift thermal cooling driving subsidence of the northern South China Sea margin since the Early Miocene (Ru and Pigott, 1986; Yu, 1994). During this phase of thermal subsidence, at ~5.3 Ma, the Dongsha Event occurred around the Dongsha Islands, involving widespread uplift and normal faulting (e.g. Lüdmann et al., 2001). Several mechanisms may have triggered the Dongsha Event, including the collision between Taiwan and the East Asian continent (Lüdmann et al., 2001; Hall, 2002), isostatic rebound (Zhao et al., 2012), post-rift magmatism (Franke, 2013), lithospheric bending (Wu et al., 2014), and/or subduction of the South China Sea beneath the Philippine Sea plate (Xie et al., 2017).

Post-spreading magmatism in the South China Sea may reflect mantle melting by residual heat and water (Clift et al., 2001), magma upwelling triggered by subduction of the South China Sea along the Manila trench and collision with Taiwan Island (Lüdmann et al., 2001), convective removal of continental lithosphere by warm asthenosphere (Lester et al., 2014), or magma upwelling from the high-velocity layer, fed by the Hainan mantle plume (Franke, 2013; Xia et al., 2016; Fan et al., 2017). Volcanoes generated by post-rift magmatism in the early Miocene-Quaternary were emplaced both onshore and offshore (e.g. Zou et al., 1995; Yan et al., 2006; Franke, 2013; Li et al., 2014; Sun et al., 2014b; Zhao et al., 2014, 2016; Fan et al., 2017), with the latter typically extruded onto the continental slope in relatively shallow water depths (<300 m; Yan et al., 2006; Zhao et al., 2016). Boreholes reveal these shallow-water volcanoes are composed of basalt, dacite, and rhyolitic tuff (Li and Liang, 1994; Yan et al., 2006; Zhao et al., 2016). In addition to the onshore and shallow-water volcanoes, several volcanoes were emplaced further basinwards on the continental slope in deeper water, close to the Continent-Ocean Boundary (COB) (Clift et al., 2001; Wang et al., 2006; Cameselle et al., 2017) (Fig. 1). We examine two of these deep-water volcanoes, which are situated in an area currently characterized by water depths of 1850–2680 m and that are now buried by sedimentary strata (e.g. Clift et al., 2001) (Figs. 1). Micropalaeontological data from the Pearl River Mouth Basin (Xu et al., 1995; Qin, 1996), and microfauna data from ODP sites 1146 and 1148, indicate the Middle Miocene (16.5 Ma) to Recent, nanofossil-bearing clays encasing the volcanoes were deposited in a deep-water setting (1.0–3.0 km; Wang et al., 2000; Clift et al., 2001).

3. Data and Methods

We use a time-migrated 3D seismic reflection survey acquired in 2012 and covering an area of ~350 km^2 (Fig. 1b). The seismic data are zero-phase processed and displayed with SEG (Society of Exploration Geophysicists) normal polarity, whereby a downward increase in acoustic impedance (a function of rock velocity and density) corresponds to a positive reflection event (red on seismic profiles) (e.g. Brown, 2004). Bin spacing is 25 m, and the seismic data have a dominant frequency in the interval of interest (i.e. 0–400 ms two-way time (twt)) of ~40 Hz.

Stacking velocities are not available for the survey and no wells intersect the studied Late Miocene-Quaternary, buried, deep-water volcanic features. We thus have no direct control on the composition or velocities of the seismically imaged volcanic materials. Depth-conversion of volcano and lava flow thickness measurements in milliseconds (twt) to meters is therefore based on velocity estimates, which introduces some uncertainty into our erupted volume calculations. To derive a reasonable velocity estimate, we use velocity data for submarine volcanoes obtained from boreholes (i.e. BY7-1 and IODP 349) (Li et al., 2015; Zhao et al., 2016) and OBS (Ocean Bottom Seismometer) profiles (Yan et al., 2001; Wang et al., 2006; Chiu, 2010; Wei et al., 2011) in the South China Sea. The boreholes, which are situated >300 km away from our study area, intersect buried basaltic volcanoes with p-wave velocities of ~4.5 km/s (BY7-1; Zhao et al., 2016) and ~3.0–5.0 km/s (IODP U1431; Li et al., 2015). OBS profiles imaging submarine volcanoes located only 140 km from the study area (Fig. 1a) typically have p-wave velocities of >3.0 km/s, and occasionally up to ~5.5 km/s (Yan et al., 2001; Wang et al., 2006; Chiu, 2010; Wei et al., 2011).

The basaltic composition and p-wave velocities of ~3.0–5.5 km/s for volcanoes intersected by boreholes and studied using OBS data are consistent with p-wave velocity data for shallow-water, mafic volcanoes located offshore western India (~3.3–5.5 km/s; Calvès et al., 2011), and offshore southern Australia in the Bight (~2.4–6.7 km/s, with an average velocity of 4.0 km/s; Magee et al. 2013) and Bass (~2.2–4.0 km/s with an average of 3.0 km/s; Reynolds et al. 2018) basins. Based on these velocity data, we assume the imaged volcanic material studied here have mafic compositions and p-wave velocities of 4.0 (±1.0) km/s. It is important to note that, using a range of estimated velocities does not affect our calculation of *relative* amount of material contained within volcanic edifices versus the flanking lava flows (Text S1; Table S1-S4).

We calculate a vertical resolution (λ/4) of ~10 m for the sedimentary strata encasing the volcanic materials, given a dominant frequency of 40 Hz and assuming a seismic velocity of 2.2 km/s for the nanofossil-bearing clay (based on seismic refraction profiles OBS1993, Yan et al., 2001; OBS2001, Wang et al., 2006; OBS2006-3, Wei et al., 2011). The calculated vertical resolution for the volcanic materials is 19-31 m, based on a dominant frequency of 40 Hz and estimated seismic velocities of 4.0 (±1.0) km/s. The top and base of volcanic structures can be distinguished in seismic reflection data when their thickness is greater than the estimated vertical resolution of these data (i.e. 19-31 m); volcanic structures with thicknesses below the vertical resolution, but above the detection limit (i.e. λ/8 = 10-16 m,) are imaged as tuned reflection packages, whereby reflections from their top and base contacts interfere on their return to the surface and cannot be distinguished (Brown, 2004). The lava flows are typically >2 seismic cycles thick (), suggesting they too are thicker than the tuning thickness and are represented by discrete top and basal reflections (Table S2-S3).

We interpreted four seismic surfaces tied to ODP Site 1146, which is located ~65 km west of the study area (Figs. 1a, 2), and two horizons locally mappable around the volcanoes: T0 (~2.58 Ma), T1 (~5.3 Ma), TRa (~6.5 Ma), and TRb (~8.2 Ma), and TM and BM, which correspond to the top and base of the volcanic materials, respectively. The youngest age of the volcanoes and associated lava flows are dated using the first seismic reflection that onlaps or overlies them (Fig. 3). After mapping TM and BM, we calculated the volumes of the volcanic features (Table S1-S4), with errors largely arising from uncertainties in the velocities (4.0±1.0 km/s) used to undertake the depth conversion (see above).

Root mean square (RMS) amplitude extractions and slices through a variance volume were used to constrain the geometry, scale, and distribution of the submarine volcanoes (Figs. 3-6). The RMS amplitude attribute computes the square root of the sum of squared amplitudes, divided by the number of samples within the specified window used; put simply, the RMS attribute measures the reflectivity of a given thickness of seismic data (Fig. 4a) (Brown, 2004). The variance attribute is free of interpreter bias because it is directly derived from the processed data (Fig. 5a). Variance measures the variability in shape between seismic traces; this can be done in a specified window along a picked horizon or within a full 3D seismic volume. Variance is typically used to map structural and stratigraphic discontinuities related to, for example, faults and channels (Brown, 2004).

4. Seismic expression and interpretation of igneous features

We identify three main types of seismic structures and associated facies: (1) Seismic Facies 1 (SF1) - two (V1 and V2) conical-shaped features up to ~202 ms twt (~404±101 m) thick, which internally are weakly-to-moderately reflective or chaotic, capped by a positive polarity, high-amplitude reflection (TM) onlapped by overlying strata (Figs. 3a, 6a). Where present, internal reflections downlap onto BM (Fig. 3a); (2) Seismic Facies 2 (SF2) - ribbon-like, broadly strata-concordant, high-amplitude, positive polarity reflections, which emanate from the conical structures (SF1) and extend up to ~9.2 km downslope (Figs. 3a-b, 5c, 6a); and (3) Seismic Facies 3 (SF3) - saucer-shaped, strata-discordant, high-amplitude reflections (Fig. 5c). The conical shape of SF1 and downlap of its internal reflections (where developed) onto BM, coupled with onlap of overlying reflections onto TM, suggest SF1 is extrusive rather than intrusive. SF1 is similar in terms of its conical shape, highly reflective top, and internally chaotic reflections to mud volcanoes documented elsewhere in the northern South China Sea (Sun et al., 2012; Yan et al., 2017);SF1 could therefore represent a mud volcano that fed long run-out mud flows (i.e. SF2). Alternatively, the highly reflective, ribbon-like geometry of SF2 is similar to that associated with shallow/free gas accumulations (Sun et al., 2012). We consider these two interpretations unlikely because: (i) the limited supply and high viscosity of mud means mud volcanoes are rarely associated with long run-out flows, although we note that one mud flow in the Indus Fan was ~5.0 km long (Calvès et al. 2009); and (ii) the top of SF2 is defined by a positive polarity reflection (downward increase in acoustic impedance), which is opposite to that typically associated with shallow/free gas accumulations (e.g. Judd and Hovland, 2007; Sun et al., 2012). Based on their geometric and geophysical characteristics, spatial relationships, and similarity to structures observed on other rifted continental margins, we interpret these features as volcanic edifices (SF1), genetically related lava flows (SF2), and saucer-shaped sills (SF3) (e.g. Berndt et al., 2000; Planke et al., 2000; Thomson and Hutton, 2004; Calvès et al., 2011; Jackson, 2012; Magee et al., 2013;

Reynolds et al., 2018). We now focus on the detailed external morphology and internal architecture of the two deep-water volcanoes that are shallowly buried (<330 m) and thus well-imaged.

4.1. Volcano edifice 1 (V1) and associated lava flows

V1 is a prominent, ~202 ms twt high (404±101 m) and ~3.0 km diameter conical volcano covering ~7.2 km^2, with a volume of ~0.94±0.24 km^3 and an average flank dip of ~15.0±3.6° (Figs. 3-4; Table S1). V1 is onlapped by overlying reflections, with the oldest onlapping reflection correlating to TRa (~6.5 Ma); this suggests V1 was emplaced in the latest Miocene-earliest Pliocene (Fig. 3a). V1 is underlain by a downward-tapering, >1.1 km deep, up to 2.0 km wide, sub-vertical zone of chaotic reflections (Fig. 3a). We attribute the poor imaging within this chaotic sub-vertical zone to: (1) the presence of sub-vertical feeder intrusions that disrupt background reflections and scatter energy (cf. Thomson, 2007); (2) increased fluid flow and hydrothermal alteration in fractured and deformed host rock adjacent to the magma plumbing system; and/or (3) scattering of energy travelling through the volcano, leading to 'wash-out' of the underlying data (i.e. a geophysical artefact; Magee et al. 2013). This reduction in imaging beneath the volcanoes partly obscures their basal surface, but where visible it is clear BM undulates and truncates underlying stratal reflections (Fig. 3b).

V1 is surrounded by an asymmetric apron of moderate-to-high amplitude reflections extending up to 1.5 km from the main edifice. The apron is up to ~115 ms twt thick (~230±58 m), and has a dip of <0.5° (Figs. 4a-b; Table S2). A package of moderate-to-very high-amplitude reflections extending a further c. 1.5 km down-dip of this apron contains very high-amplitude, channel-like geometries (C1-C3), which terminate down-dip into or are flanked at prominent bends by, moderate-amplitude, fan-like geometries (F1-F4) (Figs 1b, 4a). We interpret these two features as lava flow channels and fans, respectively (Fig. 3-4). The lava flow channels are sinuous, <340 m wide, and usually bisect the lava fans (Figs 4a-b). Lava flow-related features (i.e. apron, channels, and fans) emanating from V1 cover an area of ~14 km^2 (Tables S3-S4), have an average thickness of ~33 ms twt (~66±17 m), and a volume of ~0.92±0.23 km^3; this volume is nearly equal to that of V1 (~0.94±0.24 km^3) and thus represents ~50% of the total erupted volume (~1.86±0.47 km^3).

4. 2. Volcano edifice 2 (V2) and associated lava flows

V2 covers ~0.44 km^2 and is elliptical in plan-view, with long and short axes of ~1.2 km and ~0.6 km, respectively (Figs. 5a-b, 6a). The volcano is ~100 ms twt high (~200±50 m), with an irregular base, has flank dips of ~27.8±5.9º, and a volume of 0.03±0.01 km^3 (Figs. 5a, 6a; Table S1). The top of V2 is of moderate amplitude and is irregular, with the oldest onlapping reflections correlating to T1 (~5.3 Ma) suggesting V2 is latest Miocene-earliest Pliocene, but probably younger than V1 (Fig. 6a). Reflections within V2 are chaotic and, similar to V1, V2 is underlain by a vertical zone of disturbance (Fig. 6a). V2 lacks a lava apron, instead being directly flanked by relatively straight, up to 9.2 km long lava flow channels on its south-eastern side (C4-C7) (Fig. 5a). Lava flow C6 is unusual in that underlying strata are truncated at the base of the flow, defining 'ramps' that are up to~32.5 ms twt high (~65±16 m) high and dip towards V2 at ~25.5±5.8° (Figs. 6b-c1). Beyond the main ramp at the base of C6 (Fig. 5b), the lava flows thickens to ~130 ms twt (~260±65 m), where it is defined by stacked, high-amplitude reflections that have a lobate geometry in plan-view (F5) (Figs. 5a-b, 6a, 6c-c1). At its distal end, the pinch out of F5 occurs where it abuts a basal ramp that is ~90±23 m tall and that dips ~9.3±2.3° (Figs. 6c-c1). F5 is capped by a younger lava fan (F6) (Figs. 6c-c1). The V2-sourced lava flows (C4-C7 and F5) cover ~11.5 km^2; ~4.20 km^2 of this comprises lava flow channels and ~7.32 km^2 lava fan. Given the average thickness of the lava flow channels (~61±16 m) and fans (~109±27 m), we estimate the total volume of V2-sourced lava flows to be ~1.05±0.27 km^3; this volume estimate is ~35 times greater than that of the main V2 edifice (0.03±0.01 km^3), representing ~97% of the total erupted volume.

4.3. Shallow sills and associated lava flows

South of V2, we map two areally extensive, partly merged lava flows emanating from the upper tips of inclined sheets fringing saucer-shaped sills (i.e. S1 and S2) (Figs. 1b, 5a-c). A narrow, vertical, seismically chaotic/blanking zone occurs directly below the saucer-shaped sills (Fig. 5c). Several linear structures, rooted at the junction between sills, and feeding the overlying lava fan (F6), are also observed (Fig. 5c). F6 covers an area of ~49 km^2, with a diameter of ~7.9 km and thickness of 55±14 m (Table S4). F6 is directly onlapped by surface T0 (~2.58 Ma), suggesting it was emplaced in the latest Pliocene (Fig. 5c). Similar to other lava fans, F6 is characterized by a single, positive, high-amplitude seismic event (Fig. 5c). F6 extends beyond the seismic coverage and is much bigger than other lava fans imaged in the study area (Figs, 5; Table S4).

5. Discussion

5.1. Water depths during volcano emplacement

The different burial depths and onlap relationships of the volcano edifices and lava flows studied here suggest three phases of volcanism: i.e. ~6.5 Ma for V1, ~5.3 Ma for V2, and ~2.58 Ma for S1/S2 (Figs. 2-3, 5c, 6a). According to the micropalaeontological zones of the Pearl River Mouth Basin (Xu et al., 1995; Qin, 1996), the water depths during V1 and V2 emplacement were likely only ~75 m and ~150 m shallower than present depths of ~2.25 km and ~2.14 km, respectively. The water depth during the emplacement of F6, fed by S1/S2, was probably ~150 m greater than the present depth of ~2.32 km (Xu et al., 1995; Qin, 1996). To be conservative, we estimate that volcanism in the study area occurred in water depths of a little over 2.0 km.

5.2. Origin of post-spreading volcanism in the SCS

The volcanoes documented here are substantially younger (~6.3-2.58 Ma) than those previously observed in the central SCS (~13.8-7.0 Ma; Expedition 349 Scientists, 2014; Li et al., 2015) and on the middle-lower slope of the northern SCS (~23.8-17.0 Ma; Yan et al., 2006; Zhao et al., 2016; Fan et al., 2017). Moreover, these small-scale, buried, post-spreading volcanic features have not been identified by lower-resolution techniques (e.g. gravity, magnetism, OBS and 2D seismic data). These young volcanic features maybe widespread and diagnostic of post-spreading magmatism across the northern SCS, implying the SCS may not be magma-poor, as has previously been suggested (e.g. Briais et al., 1993; Yan et al., 2006).

Given that the volcanoes documented here were emplaced after SCS rifting (>32 Ma ago; e.g. Taylor and Hayes, 1983; Franke et al., 2014; Li et al., 2015) and spreading (>15 Ma ago; Li et al., 2014), it is clear they have a different origin to the breakup-related volcanoes described elsewhere (e.g. Yan et al., 2006; Expedition 349 Scientists, 2014; Li et al., 2015; Zhao et al., 2016; Fan et al., 2017). The post-spreading age of volcanism may suggest that mantle melting (Clift et al., 2001) and convective removal of continental lithosphere by warm asthenosphere (Lester et al., 2014), processes typically associated with rifting and breakup, were not responsible for the generation of this phase of igneous activity. Latest teleseismic imaging shows that the eastern branch of the Hainan Plume likely underlies the lower crust beneath the study area (Xia et al., 2016), suggesting plume melt (Franke, 2013; Xia et al., 2016; Fan et al., 2017) may have supplied magma to the observed volcanoes. This interpretation is also supported by the overall decrease in the age of magmatism with distance from the Hainan Plume across the SCS, from ~23.8-17.0 Ma on the proximal continental slope (Yan et al., 2006; Zhao et al., 2016; Fan et al., 2017) to ~6.30-2.58 Ma in the deeper water study area (Xia et al., 2016). Faulting associated with the Dongsha Event peaked at ~5.3 Ma and 2.58 Ma and was broadly synchronous with the main period of eruptive magmatism documented here (Lüdmann et al., 2001). Faults generated during the Dongsha Event may have provided high-permeability zones that promoted the vertical migration of magma that fed the eruptive centers.

5.3. Volcano construction

Both V1 and V2 are underlain by sub-vertical, pipe-like zones of chaotic reflections, which we suggest demarcate the limits of their magma plumbing systems. The basal surfaces of V1 and V2 truncate underlying strata (Figs. 3a, 6a). Apparent erosion of the sub-volcanic substrate may indicate the initial eruptions were explosive (cf. eye-shaped hydrothermal vents documented by, for example, Hansen et al. 2006; Magee et al. 2016). Alternatively, the basal surface may appear erosive due to sinking of the volcano into the underlying, wet, unconsolidated sediments. Internal reflections that lie sub-parallel to the flanks of V1 and V2 suggest the volcanoes grew by increasing both edifice height and diameter by the accretion of volcanic material (Magee et al. 2013). Flank dips of ~15-28° likely indicate that the volcanic material building the edifices constitutes coherent lava flows and/or a dome structure, rather than a pyroclastic cone of tephra (Francis and Thorpe, 1974; Griffiths and Fink, 1992). Construction via emplacement of coherent lava flows is consistent with the presence of internal reflections in V1 and V2; i.e. boundaries between blocky lava flows would be irregular and scatter seismic energy, meaning they would not likely be imaged.

5.4. Lava flow extrusion dynamics

In addition to the formation of volcanic edifices, both V1 and V2, as well as S1 and S2, are associated with extensive lava flows. In particular, we show V1 and V2 are flanked either by an asymmetric lava apron, which is broader on their downslope (SE) side, or lava flow channels that flowed south-eastwards for up to >9 km (Figs. 3a, 4a-b, 5a). At sub-aerial volcanoes (e.g. Walker, 1993; Cashman et al., 1999), high eruption rates and low magma viscosities are the dominant causes of long run-out lava flows. Extensive lava flows have also been observed at other deep-water volcanoes (e.g. Chadwick et al., 2018; Embley and Rubin; Ikegami et al., 2018) and occur primarily because of the high hydrostatic pressure in deep-water environments. Higher ambient pressure can affect lava rheology (lower viscosity, vesicularity, crystal content), suppress magma decompression and ascent, and, thereby, extrusion dynamics (Bridges, 1997; Gregg and Fornari, 1998). For example, upon eruption of a 1200-1100°C basalt (MORB composition) at a confining pressure of 20 MPa (i.e. a hydrostatic-equivalent water depth of 2 km), lava can contain up to 1.4 wt% H_2O at equilibrium volatile solubility (Newman and Lowenstern, 2002). The resulting lava viscosity of 9-38 Pa s is significantly lower than a dry (0.1 wt% H_2O) sub-aerial basalt, having a viscosity range of 41-248 Pa s (calculated using Giordano et al., 2008). Higher H_2O content in lavas erupted in deep-water, compared to those extruded in sub-aerial settings, will also mean: (1) there are fewer bubbles or fragmentation to hinder flow because there is less degassing (Gregg and Fornari, 1998); (2) crystallization may be inhibited, reducing the effect of crystal interactions on viscosity; and (3) the glass transition temperature is suppressed (Giordano et al. 2008), allowing lavas to flow further.

From our seismic reflection data it is also clear channelization in lava tubes, in addition to the water content effects described above, also facilitated long distance lava transport. We suggest these tubes formed by rapid cooling and hardening of a surficial crust that insulated and focused lava flow through a core channel (e.g. Cashman et al., 1999). Based on the long run-out lava distances, we consider our initial assumption that the imaged volcanic features have a mafic composition remains valid. Overall, whilst we do not know the composition of the lavas imaged in our seismic reflection data, pressure-related changes in lava rheology and channelization of any lava type (i.e. mafic to silicic) will allow it to flow hotter for longer. Given the downslope topographic controls during eruption, a combination of rheology changes and channelization allowed lavas to flow for >9 km from associated volcanic edifices.

The overall geometry and internal architecture of the imaged lava flows indicate substrate rheology was a key control on emplacement dynamics. Our 3D seismic reflection data show that relatively long run-out lava flows (>9 km) erupted from deep-water volcanoes have a rugged basal surface that is locally defined by erosional basal 'ramps'. Truncation of underlying strata suggests the lavas were able to erode down into the seabed, perhaps because the pre-eruption substrate was cold, wet, and unconsolidated. We suggest erosion of the lava substrate was promoted by: (1) the dense (vesicle-poor) lava sinking down into or 'dredging' the soft sediments (Duffield et al., 1986; Ikegami et al. 2018); (2) thermal erosion (Griffiths, 2000); and/or (3) more "turbulent" flow dynamics of channelized lava, consistent with the inferred low viscosities (<10 Pa s).

Lava flow eventually ceased in distal areas due to gradual cooling and crystallization (Cashman et al., 1999). We suggest that, in the case of the straight lava flows (C5 and C6), lava transported within the axial tube temporarily accumulated at the transient end of the flow, possibly forming a lava pool (Greeley, 1987). Lava entering the tube from the ongoing or new volcanic eruption caused an increase in pressure, with the cooled and crystallized material at the flow toe forming an impermeable, albeit, transient barrier. High hydrostatic pressure (>26 MPa at C5 and C6) and thick surficial crusts inhibited the release of pressure build up by significant lava inflation (Gregg and Fornari, 1998). Eventually, pressure build-up was sufficient to rupture this frontal, leading to emplacement of a fan downdip of the front-most base-lava ramp (F5; Fig. 5a, 6) (Griffiths, 2000). However, in the case of fans (e.g. F1-4) fed by sinuous channels (Figs. 4a-b), we suggest these were emplaced in a process similar to that documented by Miles and Cartwright (2010), with lobate lava flows fed and bisected by a 'lava tube' through magma inflation and increases in eruption rate. At the end of sinuous lava flow channels (e.g. C1), the main channel bifurcated to form a lobate fan (F3, Figs. 4a-b), which was also probably caused by flow branching triggered by magma cooling (Griffiths, 2000).

5.5. Volume balance of volcano edifice and lava flow

Inaccurate constraints on total erupted volumes compromises our understanding of volcano construction, lava propagation, eruption rates, eruption durations, magma storage conditions, melting processes, and risk assessment of volcanism in deep-water settings (Carey et al., 2018). High-resolution 3D seismic reflection data allow us to calculate the volumes of material contained within volcano edifices and in flanking lava flows. We show that most (i.e. 50-97%) of the erupted material is transported away from the imaged edifices, an observation comparable to that made for deep-ocean volcanic eruptions (Caress et al., 2012; Carey et al., 2018). A critical outcome of our work is that flanking lava flows, and to a lesser extent the volcanic edifices, have rugged and discordant bases (Fig. 6a); accurately calculating the volume of deep-water volcanoes and lava flows therefore requires an understanding of their basal morphology. Erupted volume estimates based solely on remote sensing of the seabed may be thus incorrect (e.g. Robinson and Eakins, 2006). Although we show the accuracy of total erupted volume estimates can be improved by constraining basal volcano and lava morphologies, seismic images capturing the geological record of deep-water volcanoes cannot determine how much, if any, volcanic material was transported away from the eruption site as pumice rafts (e.g. Carey et al. 2018). Nevertheless, 3D seismic imaging can significantly improve quantitative volume estimates of recent and ancient volcanic features (e.g. volcano edifices and lava flows) either currently on the seafloor or now buried by sedimentary successions.

6. Conclusions

High-resolution 3-D seismic data from the South China Sea allow us to image and map the internal structure, calculate the volume of erupted material, and to better understand the extrusion dynamics of buried deep-water volcanoes; such insights cannot readily be gained from analysis of remote sensing data. Volcanism occurred ~6.3-2.58 Ma, after seafloor spreading had ceased in the area, and may be related to the Hainan mantle plume. High hydrostatic pressure, an inclined seabed, and low-strength, very fine-grained, near-seabed sediments, combined with formation of lava tubes and extrusion of low-viscosity magmas, are likely responsible for observed long-distance lava run-outs (>9 km) in this deep-water environment. We show the imaged volcanic edifices and associated lava flows have rugged, erosional bases, meaning traditional remote sensing-based volume calculations of deep-water volcanic features, which typically assume smooth bases, are underestimated. Because seismic reflection data images the base of deep-water volcanoes and lava flows, we calculate a large amount (as high as ~97%) of the erupted materials are transported away from the volcano edifices, suggesting that volume of deep-water volcanic edifices may not faithfully archive eruption size or magma production. Considering deep-water conditions (e.g. high hydrostatic pressure and unconsolidated sediments) in the study area are common elsewhere, the conclusions derived from this study can likely be used in other deep-water sedimentary basins and some mid-ocean ridges. Our study highlights that 3D seismic reflection data can play a critical to understanding volcano morphology in 3D and accurately estimating volume of erupted material.

Acknowledgment

This work was supported by the National Scientific Foundation of China (Grant Nos. 91528301, 41676051 and 41372112), the Programme of Introducing Talents of Discipline to Universities (No. B14031) and the Fundamental Research Funds for the Central Universities-the China University of Geosciences (Wuhan) (No. CUG160604). We thank the China National Offshore Oil Company

(CNOOC) for permission to release the data; reflection seismic data may be requested from CNOOC (http://www.cnooc.com.cn/en/). Editor Uri ten Brink and Reviewers Dieter Franke, Gerome Calvès and Nick Schofield are thanked for their invaluable comments and suggestions. We also appreciate Dennis Brown for his comments on an earlier version of this paper. Rebecca Bell is thanked for generously providing office space during the visit of Qiliang Sun to Imperial College. Chunfeng Li from the Zhejiang University and Chaoyan Fan from the South China Sea Institute of Oceanology, Chinese Academy of Sciences are appreciated for their discussion during the paper preparation and revision.

References

Allen, R.W., Berry, C., Henstock, T.J., Collier, J.S., Dondin, F.J-Y., Rietbrock, A., Latchman, J.L., and Robertson, R.E.A., 2018, 30 Years in the Life of an Active Submarine Volcano: A Time - Lapse Bathymetry Study of the Kick-'em-Jenny Volcano, Lesser Antilles: Geochemistry, Geophysics, Geosystems, v. 19, p. 715-731, doi: doi.org/10.1002/2017GC007270.

Berndt, C., Skogly, O.P., Planke, S., Eldholm, O., and Mjelde, R., 2000, High-velocity break up-related sills in the Vøring Basin, off Norway. Journal of Geophysical Research-Solid Earth, v. 105, p. 28443-28454, doi: 10.1029/2000JB900217.

Briais, A., Patriat, P., and Tapponnier, P., 1993, Updated interpretation of magnetic anomalies and seafloor spreading stages in the South China Sea: Implications for the Tertiary tectonics of Southeast Asia: Journal of Geophysical Research, v. 98, p. 6299-6328, doi:10.1029/92JB02280.

Bridges, N.T., 1997, Ambient effects on basalt and rhyolite lavas under Venusian, subaerial, and subaqueous conditions. Journal of Geophysical Research: Planets, v. 102(E4), p. 9243-9255, doi: 10.1029/97JE00390.

Brown, A.R., 2004, Interpretation of three-dimensional seismic data: AAPG Memoir 42, 6thed. SEG Investigations in Geophysics.

Calvès, G., Schwab, A.M., Huuse, M., Clift, P.D., Gaina, C., Jolley, D., Tabrez, A.R., and Inam, A., 2011, Seismic volcanostratigraphy of the western Indian rifted margin: The pre-Deccan igneous province: Journal of Geophysical Research, v. 116, p. B01101, doi:10.1029/2010JB000862.

Calvès, G., Schwab, A.M., Huuse, M., van Rensbergen, P., Clift, P.D., Tabrez, A.R., and Inam, A., 2009, Cenozoic mud volcanoe activity along the Indus Fan: offshore Pakistan: Basin Research, v. 22, p. 398-413, doi: 10.1111/j.1365-2117.2009.00448.x.

Cameselle, A.L., Ranero, C.R., Franke, D., and Barckhausen, U., 2017, The continent-ocean transition on the northwestern South China Sea: Basin Research, v. 29, p. 73-95, doi: 10.1111/bre.12137.

Caress, D.W., Clague, D.A., Paduan, J.B., Martin, J.F., Dreyer, B.M., Chadwick Jr, W.W., Denny, A., and Kelley, D.S., 2012, Repeat bathymetric surveys at 1-metre resolution of lava flows erupted at Axial Seamount in April 2011: Nature Geoscience, v. 5, p. 483-488, doi: 10.1038/NGEO1496.

Carey, R., Soule, S.A., Manga, M., White, J.D.L., McPhie, J., Wysoczanski, R., Jutzeler, M., Tani, K., Yoerger, D., Fornari, D., Caratori-Tontini, F., Houghton, B., Mitchell, S., Ikegami, F., Conway, C., Murch, A., Fauria, K., Jones, M., Cahalan, R., and McKenzie, W., 2018. The largest deep-ocean silicic volcanic eruption of the past century: Science Advances, v. 4, p. e1701121, doi: 10.1126/sciadv.1701121.

Cashman, K.V., Thornber, C.R., and Kauahikaua, J.P., 1999, Cooling and crystallization of lava in open channels, and the transition of pahoehoe lava to `a`a: Bulletin of Volcanology, v. 61, p. 306-323, doi: 10.1007/s004450050.

Chadwick Jr, W.W., Merle, S.G., Baker, E.T., Walker, S.L., Resing, J.A., Butterfield, D.A., Anderson, M.O., Baumberger, T. and Bobbitt, A.M., 2018, A recent volcanic eruption discovered on the central Mariana back-arc spreading center: Frontiers in Earth Science, v. 6, p. 172, doi: 10.3389/feart.2018.00172.

Chiu, M., 2010, The p-wave velocity modeling of the transitional crust in northern South China Sea continental margin: National Taiwan Ocean University, Keelung.

Clift, P.D., Lin, J., and ODP Leg 184 Scientific Party, 2001, Patterns of extension and magmatism along the continent-ocean boundary, South China margin: Geological Society, London, Special Publications, v. 187, p. 489-510, doi: 10.1144/GSL.SP.2001.187.01.24.

Cocchi, L., Masetti, G., Muccini, F., and Carmisciano, C., 2016, Geophysical mapping of Vercelli Seamount: Implications for Miocene evolution of the Tyrrhenian back arc basin: Geoscience Frontiers, v. 7, p. 835-849, doi: 10.1016/j.gsf.2015.06.006.

Ding, W.W., and Li, J.B., 2016, Propagated rifting in the Southwest Sub-basin, South China Sea: Insights from analogue modelling: Journal of Geodynamics, v. 100, p. 71-86, doi:10.1016/j.jog.2016.02.004.

Duffield, W.A., Bacon, C.R., and Delaney, P.T., 1986, Deformation of poorly consolidated sediment during shallow emplacement of a basalt sill, Coso Range, California: Bulletin of Volcanology, v. 48, p. 97-107, doi: 10.1007/BF01046545.

Embley, R.W. and Rubin, K.H., 2018, Extensive young silicic volcanism produces large deep submarine lava flows in the NE Lau Basin: Bulletin of Volcanology, v. 80, n. 4, p. 36, doi: 10.1007/s00445-018-1211-7.

Expedition 349 Scientists, 2014, South China Sea tectonics: Opening of the South China Sea and its implications for southeast Asian tectonics, climates, and deep mantle processes since the late Mesozoic: International Ocean Discovery Program Preliminary Report, v. 349, doi:10.14379/iodp.pr.349.2014.

Fan, C.Y., Xia, S.H., Zhao, F., Sun, J.L., Cao, J.H., Xu, H.L., and Wan, K.Y., 2017, New insights into the magmatism in the northern margin of the South China Sea: Spatial features and volume of intraplate seamounts: Geochemistry, Geophysics, Geosystems, v. 18, p. 2216-2239, doi:10.1002/2016GC006792.

Francis, P.W. and Thorpe, R.S., 1974. Significance of lithologic and morphologic variations of pyroclastic cones:

Geological Society of America Bulletin, v. 85, n. 6, p. 927-930, doi: 10.1130/0016-7606(1974)85<927:SOLAMV>2.0.CO;2.

Franke, D., 2013, Rifting, lithosphere breakup and volcanism: comparison of magma-poor and volcanic rifted margins: Marine and Petroleum Geology, v. 43, p. 63-87, doi: 10.1016/j.marpetgeo.2012.11.003.

Franke, D., Savva,D., Pubellier, M., Steuer, S., Mouly, B., Auxietre, J., Meresse, F., and Chamot-Rooke, N., 2014, The final rifting evolution in the South China Sea: Marine and Petroleum Geology, v. 58, p. 704-720, doi: 10.1016/j.marpetgeo.2013.11.020.

Funck, T., 1996, Structure of the volcanic apron north of Gran Canaria deduced from reflection seismic, bathymetric and borehole data: Ph.D. dissertation, University of Kiel.

Giordano, D., Russell, J.K., Dingwell, D.B., 2008. Viscosity of magmatic liquids: a model. Earth and Planetary Science Letters, v. 271, p. 123-134, doi: 10.1016/j.epsl.2008.03.038.

Goto, Y., and McPhie, J., 2004, Morphology and propagation styles of Miocene submarine basanite lavas at Stanley, northwestern Tasmania, Australia: Journal of Volcanology and Geothermal Research, v. 130, p. 307-328, doi: 10.1016/S0377-0273(03)00311-1.

Grosse, P., and Kervyn, M., 2018, Morphometry of terrestrial shield volcanoes: Geomorphology, v. 304, p. 1-14, doi: 10.1016/j.geomorph.2017.12.017.

Greeley, R., 1987, The role of lava tubes in Hawaiian volcanoes, U.S. Geological Survey Professional Paper 1350, p. 1589-1602.

Gregg, T.K.P., and Fornari, D.J., 1998, Long submarine lava flows: Observations and results from numerical modeling: Journal of Geophysical Research, v. 103, p. 27517-27531, doi: 10.1029/98JB02465.

Griffiths, R.W. and Fink, J.H., 1992, Solidification and morphology of submarine lavas: A dependence on extrusion rate: Journal of Geophysical Research: Solid Earth, v. 97(B13), p. 19729-19737, doi:

10.1029/92JB01594.

Griffiths, R.W., 2000, The Dynamics of lava flows: Annual Review of Fluid Mechanics, v. 32, p. 477-518, doi: 10.1146/annurev.fluid.32.1.477.

Hall, R., 2002, Cenozoic geological and plate tectonic evolution of SE Asia and the SW Pacific: Computer-based reconstructions, model and animations: Journal of Asian Earth Sciences, v. 20, p. 353-431, doi: 10.1016/S1367-9120(01)00069-4.

Holcomb, R.T., Moore, J.G., Lipman, P.W., and Belderson, R.H., 1988, Voluminous submarine lava flows from Hawaiian volcanoes: Geology, v. 16, p. 400-404, doi: 10.1130/0091-7613(1988)016<0400:VSlava flow fanH>2.3.CO;2.

Ikegami, F., McPhie, J., Carey, R., Mundana, R., Soule, S.A. and Jutzeler, M., 2018, The eruption of submarine rhyolite lavas and domes in the deep ocean–Havre 2012, Kermadec Arc: Frontiers in earth science, v. 6, n. 147, doi: 10.3389/feart.2018.00147.

Jackson, C.A.-L., 2012, Seismic reflection imaging and controls on the preservation of ancient sill-fed magmatic vents: Journal of the Geological Society, London: v. 169, p. 503-506,doi: 10.1144/0016-76492011-147.

Judd, A.G., and Hovland, M., 2007, Seabed Fluid Flow: The Impact on Geology, Biology and the Marine Environment. Cambridge University Press, Cambridge, pp. 163-178.

Lester, R., Van Avendonk, H.J.A., McIntosh, K., Lavier, L., Liu, C.S., Wang, T.K., and Wu, F., 2014, Rifting and magmatism in the northeastern South China Sea from wide-angle tomography and seismic reflection imaging: Journal of Geophysical Research: Solid Earth, v. 119, p. 2305-2323, doi: 10.1002/2013JB010639.

Li, C.F., Lin, J., Kulhanek, D.K., and the Expedition 349 Scientists, 2015, Proceedings of the International Ocean Discovery Program, v. 349, doi:10.14379/iodp.proc.349.103.2015.

Li, C.F., Xu, X., Lin, J., Sun, Z., et al., 2014, Ages and magnetic structures of the South China Sea constrained by the deep tow magnetic surveys and IODP Expedition 349: Geochemistry, Geophysics, Geosystems, v. 15, p. 4958-4983, doi: 10.1002/2014JB011686.

Li, P., and Liang, H., 1994. Cenozoic magmatism in the Pearl River Mouth Basin and its relationship to the basin evolution and petroleum accumulation: Guangdong Geology, v. 9, p. 23-34 (in Chinese with English abstract).

Lüdmann, T., Wong, H.K., and Wang, P., 2001, Plio-Quaternary sedimentation processes and neotectonics of the northern continental margin of the South China Sea: Marine Geology, v. 172, p. 331-356, doi: 10.1016/S0025-3227(00)00129-8.

Magee, C., Hunt-Stewart, E., and Jackson, C.A.-L., 2013, Volcano growth mechanisms and the role of sub-volcanic intrusions: Insights from 2D seismic reflection data: Earth and Planetary Science Letters, v. 373, p. 41-53, doi: 10.1016/j.epsl.2013.04.041.

Miles, A., and Cartwright, J., 2010, Hybrid flow sills: A new mode of igneous sheet intrusion: Geology, v. 38, p. 343-346, doi: 10.1130/G30414.1.

Newman, S., Lowenstern, J.B., 2002, VolatileCalc: a silicate melt-H_2O-CO_2 solution model written in Visual Basic for excel. Computers & Geosciences, v. 28, p. 597-604.

Planke, S., Symonds, P., Alvestad, E., and Skogseid, J., 2000, Seismic volcanostratigraphy of large-volume basaltic extrusive complexes on rifted margins: Journal of Geophysical Research, v. 105, p. 19335-19351, doi: 10.1029/1999JB900005.

Qin, G.Q., 1996, Application of micropaleontology to the sequence stratigraphic studies of late Cenozoic in the Pearl River Mouth Basin: Marine Geology& Quaternary Geology, v. 16, p. 1-18, doi: 10.16562/j.cnki.0256-1492.199.04.001.

Reynolds, P., Holford, S., Schofield, N., and Ross, A., 2017, Three-dimensional seismic imaging of ancient submarine lava flows: an example from the southern Australian margin: Geochemistry, Geophysics, Geosystems,

v. 18, p. 3840-3853, doi: 10.1002/2017GC007178.

Reynolds, P., Schofield, N., Brown, R.J. and Holford, S.P., 2018, The architecture of submarine monogenetic volcanoes-insights from 3D seismic data: Basin Research, v. 30, p.437-451, doi:10.1111/bre.12230.

Robinson, J.E., and Eakins, B.W., 2006, Calculated volumes of individual shield volcanoes at the young end of the Hawaiian Ridge: Journal of Volcanology and Geothermal Research, v. 151, p. 309-617, doi: 10.1016/j.jvolgeores.2005.07.033.

Ru, K., and Pigott, J.D., 1986, Episodic rifting and subsidence in the South China Sea: AAPG Bulletin, v. 9, p. 1136-1155.

Sibuet, J.-C., Yeh, Y.-C., and Lee, C.-S., 2016. Geodynamics of the South China Sea: Tectonophysics, v. 692, p. 98-119, doi:10.1016/j.tecto.2016.02.022

Somoza, L., Gonzalez, F.J., Barker, S.J., Madureira, P., Medialdea, T., de Ignacio, C., Lourenco, N., Leon, R., Vazquez, J.T., and Palomino, D., 2017, Evolution of submarine eruptive activity during the 2011-2012 El Hierro event as documented by hydroacoustic images and remotely operated vehicle observations: Geochemistry, Geophysics, Geosystems, v. 18, p. 3109-3137, doi: 10.1002/2016GC006733.

Sun, Q.L., Xie, X.N., Piper, D.J.W., Wu, J., and Wu, S.G., 2017, Three dimensional seismic anatomy of multi-stage mass transport deposits in the Pearl River Mouth Basin, northern South China Sea: Their ages and kinematics: Marine Geology, v. 393, p. 93-108, doi: 10.1016/j.margeo.2017.05.005.

Sun, Q.L., Wu, S.G., Cartwright, J., Wang, S.H., Lu, Y.T., Chen, D.X., and Dong, D.D., 2014b, Neogene igneous intrusions in the northern South China Sea: evidence from high resolution three dimensional seismic data: Marine and Petroleum Geology, v. 54, p. 83-95, doi: 10.1016/j.marpetgeo.2014.02.014.

Sun, Q.L., Wu, S.G., Cartwright, J., and Dong, D.D., 2012, Shallow gas and focused fluid flow systems in the Pearl River Mouth Basin, northern South China Sea: Marine Geology, v. 315-318, p. 1-14, doi:

10.1016/j.margeo.2012.05.003.

Sun, Z., Xu, Z., Sun, L., Pang, X., Yan, C., Li, Y., Zhao, Z., Wang, Z., Zhang, C., 2014a, The mechanism of post-rift fault activities in the Baiyun Sag, Pearl River Mouth Basin. Journal of Asian Earth Sciences, 89:76-87, doi: 10.1016/j.jseaes.2014.02.018.

Taylor, B., and Hayes, D.E., 1983, Origin and history of the South China Sea Basin. In: Hayes, D.E. (Ed.), The Tectonic and Geologic Evolution of Southeast Asian Seas and Islands. AGU, Washington, DC, pp. 23-56.

Thomson, K., 2007, Determining magma flow in sills, dykes and laccoliths and their implications for sill emplacement mechanisms: Bulletin of Volcanology, v. 70, p. 183-201, doi: 10.1007/s00445-007-0131-8.

Thomson, K., and Hutton, D., 2004, Geometry and growth of sill complexes: Insights using 3-Dseismic from the North Rockall Trough: Bulletin of Volcanology, v. 66, p. 364–375, doi: 10.1007/s00445-003-0320-z.

Wang, T.K., Chen, M.K., Lee, C.S., and Xia, K.Y., 2006, Seismic imaging of the transitional crust across the northeastern margin of the South China Sea: Tectonophysics, v. 412, p. 237-254, doi: 10.1016/j.tecto.2005.10.039.

Wang, P., Prell, W.L., and ODP 184 scientists., 2000, Proceedings of the Ocean Drilling Program, Initial Reports, 184. Ocean Drilling Program, College Station, TX 2000.

Walker, G.P.L., 1993, Basaltic-volcano systems. In Magmatic Processes and Plate Tectonics, edited by Pritchard, H.M., Alabaster, T., Harris, N.B.W., Neary, C.R., Geological Society Special Publication, 76: 3-38.

Wei, X.D., Ruan, A.G., Zhao, M.H., Qiu, X.L., Li, J.B., Zhu, J.J., Wu, Z.L., and Ding, W.W., 2011, A wide-angle OBS profile across the Dongsha uplift and Chaoshan depression in the mid-northern South China Sea: Chinese Journal of Geophysics, v. 54, p. 3325-3335, doi: 10.3969/j.issn.0001-5733.2011.12.030.

Wu, S.G., Gao, J.W., Zhao, S.J., Lüdmann, T., Chen, D.X., and Spence, G., 2014, Post-rift uplift and focused fluid flow in the passive margin of Northern South China Sea: Tectonophysics, v. 615-616, p. 27-39, doi:

10.1016/j.tecto.2013.12.013.

Xia, S.H., Zhao, D.P., Sun, J.L., and Huang, H.B., 2016, Teleseismic imaging of the mantle beneath southernmost China: new insights into the Hainan plume: Gondwana Research, v. 36, p. 33-43, doi: 10.1016/j.gr.2016.05.003.

Xie, Z.Y., Sun, L.T., Pang, X., Zheng, J.Y., and Sun, Z., 2017, Origin of the Dongsha Event in the South China Sea: Marine Geophysical Research, v. 38, p. 357-371, doi: 10.1007/s11001-017-9321-8.

Xu, S.C., Yang, S.K., and Huang, L.F., 1995, The application of sequence stratigraphy to stratigraphic correlation: Earth Science Frontiers, v. 2, p. 115-123.

Yan, P., Deng, H., Liu, H.L., Zhang, Z., and Jiang, Y., 2006, The temporal and spatial distribution of volcanism in the South China Sea region: Journal of Asian Earth Sciences, v. 27, p. 647-659, doi: 10.1016/j.jseaes.2005.06.005.

Yan, P., Wang, Y.L., Liu, J., Zhong, G.J., and Liu, X.J., 2017, Discovery of the southwest Dongsha Island mud volcanoes amid the northern margin of the South China Sea: Marine and Petroleum Geology, v. 88, p. 858-870, doi: 10.1016/j.marpetgeo.2017.09.021.

Yan, P., Zhou, D., and Liu, Z.S., 2001, A crustal structure profile across the northern continental margin of the South China Sea: Tectonophysics, v. 338, p. 1-21, doi: 10.1016/S0040-1951(01)00062-2.

Yang, S., Qiu, Y., and Zhu, B., 2015, Atlas of Geology and Geophysics of the South China Sea: China Navigation Publications, Tianjin.

Yu, H.S., 1994, Structure, stratigraphy and basin subsidence of Tertiary basins along the Chinese southeastern continental margin: Tectonophysics, v. 253, p. 63-76.

Zhao, F., Alves, T.M., Wu, S.G., Li, W., Huuse, M., Mi, L.J., Sun, Q.L., and Ma, B.J., 2016, Prolonged post-rift magmatism on highly extended crust of divergent continental margins (Baiyun Sag, South China Sea): Earth and Planetary Science Letters, v. 445, p. 79-91, doi: 10.1016/j.epsl.2016.04.001.

Zhao, F., Wu, S.G., Sun, Q.L., Huuse, M., Li, W., and Wang, Z.J., 2014, Submarine volcanic mounds in the Pearl River Mouth Basin, northern South China Sea: Marine Geology, v. 355, p. 162-172, doi: 10.1016./j.margeo.2014.05.018.

Zhao, S.J., Wu, S.G., Shi, H.S., Dong, D.D., Chen, D.X., and Wang, Y., 2012, Structures and dynamic mechanism related to the Dongsha Event at the northern margin of the South China Sea. Progress in Geophysics, v. 27, p. 1008-1019, doi: 10.6038/j.issn.1004-2903.2012.03.022.

Zou, H., Li, P., and Rao, C., 1995, Geochemistry of Cenozoic volcanic rocks in Zhu Jiangkou Basin and its geodynamic significance: Geochimica, v. 24, p. 33-45.

Figure Captions

Figure 1: Geological setting of the study area. (a) Bottom left: regional setting of the South China Sea that is bounded by the Red River Strike-slip faults (RRFs) to the west and by the subduction trench (Manila Trench) to the east. The study area (marked with red square) is located to the south of Dongsha Islands. The green dashed line outlines the boundary of Pearl River Mouth Basin. Locations of boreholes (Exploration well BY7-1 and ODP sites 1146 and 1148), crustal structure profiles (OBS1993 (Yan et al., 2001), OBS2001 (Wang et al., 2006), OBS2006-3 (Wei et al., 2011), and OBS2008 (Chiu, 2010)) and mud volcanoes (Mvs; Sun et al., 2012; Yan et al., 2017) are labeled. Ds = Dongsha Islands; COB = Continent ocean boundary (Adopted from Sibuet et al., 2016).The base map is modified from Yang et al. (2015); (b) Seabed morphologies of the study area. Distributions of volcano edifices (red), sills (blue), lava flows (green) and locations of Figures 4a and5a are labeled. The contour lines are in 100 ms (twt).

Figure 2: (a) Synthetic seismogram of ODP Site 1146 (Modified from Sun et al., 2017); (b) Seismic profile crossing through ODP Site 1146. The four seismic surfaces (T0 (~2.58 Ma), T1 (~5.3 Ma), TRa (~6.5 Ma) and TRb (~8.2 Ma)) are labeled. D/T =Depth/time; DT =interval transit time; RHOB = lithologic density; RC = refection coefficient; (c) Lithology and depositional environment (DE) of ODP Site 1146 (Modified from Wang et al. (2000) and Clift et al. (2001)).

Figure 3: Seismic characteristics of deep-water volcano (V1) and associated lava flow channels/fans. (a) Seismic profile crosscuts the volcano edifice and associated lava flow. See Figure S1 for the un-interpreted version of this profile; (b) Seismic profile crosscuts the lava flow (enhanced seismic anomalies). TM = top of volcano/lava flow; BM = base of volcano/lava flow;

Figure 4: (a) and (b) RMS amplitude map (± 30 ms along the surface BM) and its interpretations. Volcanic apron, lava flow channels/fans are labeled.

Figure 5: Seismic characteristics of lava flow channels/fans fed by V2 and S1/S2. (a) and (b) Variance slice (extracted from the surface BM) and its interpretations. C = lava flow channel; S = shallow sill; F = lava fan; (c) Seismic profile shows magma pluming system from deep-seated sill, shallow sills and lava fan.

Figure 6: (a) Seismic profile crosscuts V2 and along lava flow channel (C6) and Lava fans (F5 and F6). The V2 has a sharp boundary to the upslope. See location in Figure 5a. (b) and (b1)

Enlargement of the end of lava flow channel (ramp structure) and its line drawings; (c) and (c1) Enlargement and its line drawings of the lava fans (F5 and F6).TM = top of volcano/lava flow; BM = base of volcano/lava flow; See Figure S1 for the un-interpreted version of these profiles.

Figure 1

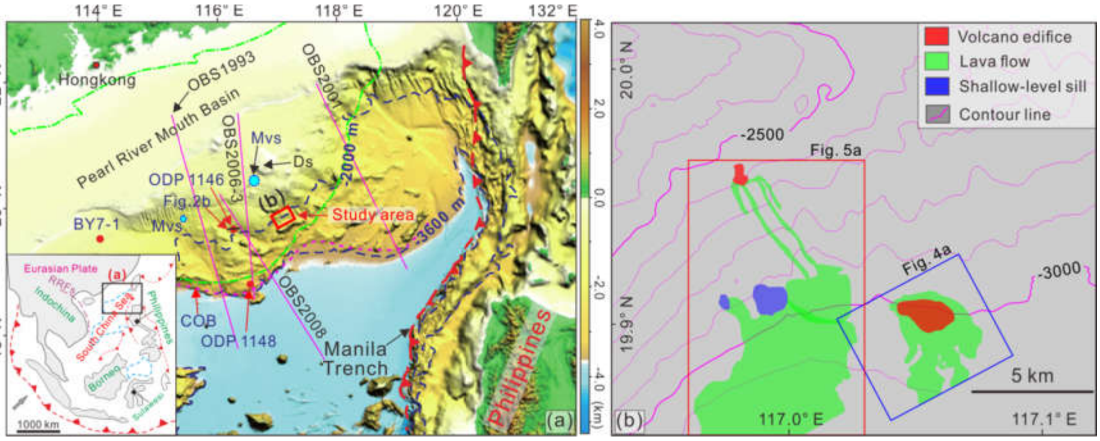
114° E
116° E
118° E
120° E
132° E
22° N
20° N
18° N
Hongkong
OBS1993
Pearl River Mouth Basin
OBS2006-3
OBS2001
Mvs
Ds
2000 m
ODP 1146
Fig. 2b
(b)
Study area
BY7-1
Mvs
3600 m
COB
ODP 1148
OBS2008
Manila Trench
Philippines
Eurasian Plate
(a)
RRFs
Indochina
South China Sea
Philippines
Borneo
Sulawesi
1000 km
4.0
2.0
0.0
-2.0
-4.0
(km)
(a)
20.0° N
19.9° N
-2500
Fig. 5a
Volcano edifice
Lava flow
Shallow-level sill
Contour line
Fig. 4a
-3000
5 km
(b)
117.0° E
117.1° E

Figure 2

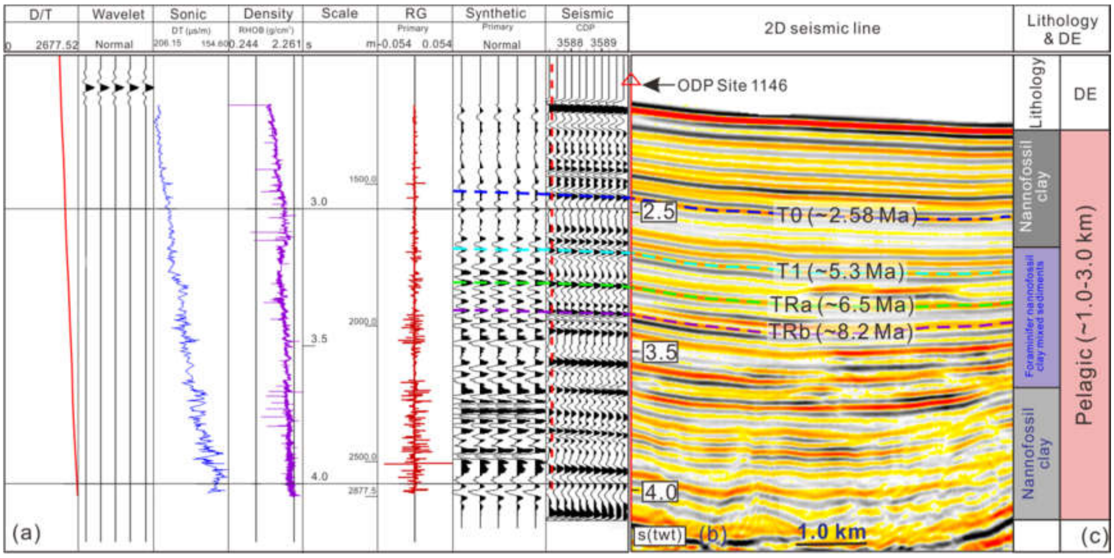

D/T
Wavelet
Sonic
Density
Scale
RG
Synthetic
Seismic
2D seismic line
Lithology & DE
2677.52
Normal
DT (μs/m)
206.15
154.60
RHOB (g/cm³)
0.244
2.261
s
m
Primary
-0.054
0.054
Primary
Normal
CDP
3588
3589
ODP Site 1146
Lithology
DE
1500.0
3.0
2.5
T0 (~2.58 Ma)
T1 (~5.3 Ma)
TRa (~6.5 Ma)
2000.0
TRb (~8.2 Ma)
3.5
2500.0
4.0
2877.5
Nannofossil clay
Foraminifer nannofossil clay mixed sediments
Nannofossil clay
Pelagic (~1.0-3.0 km)
(a)
s(twt)
(b)
1.0 km
(c)

672 Figure 3

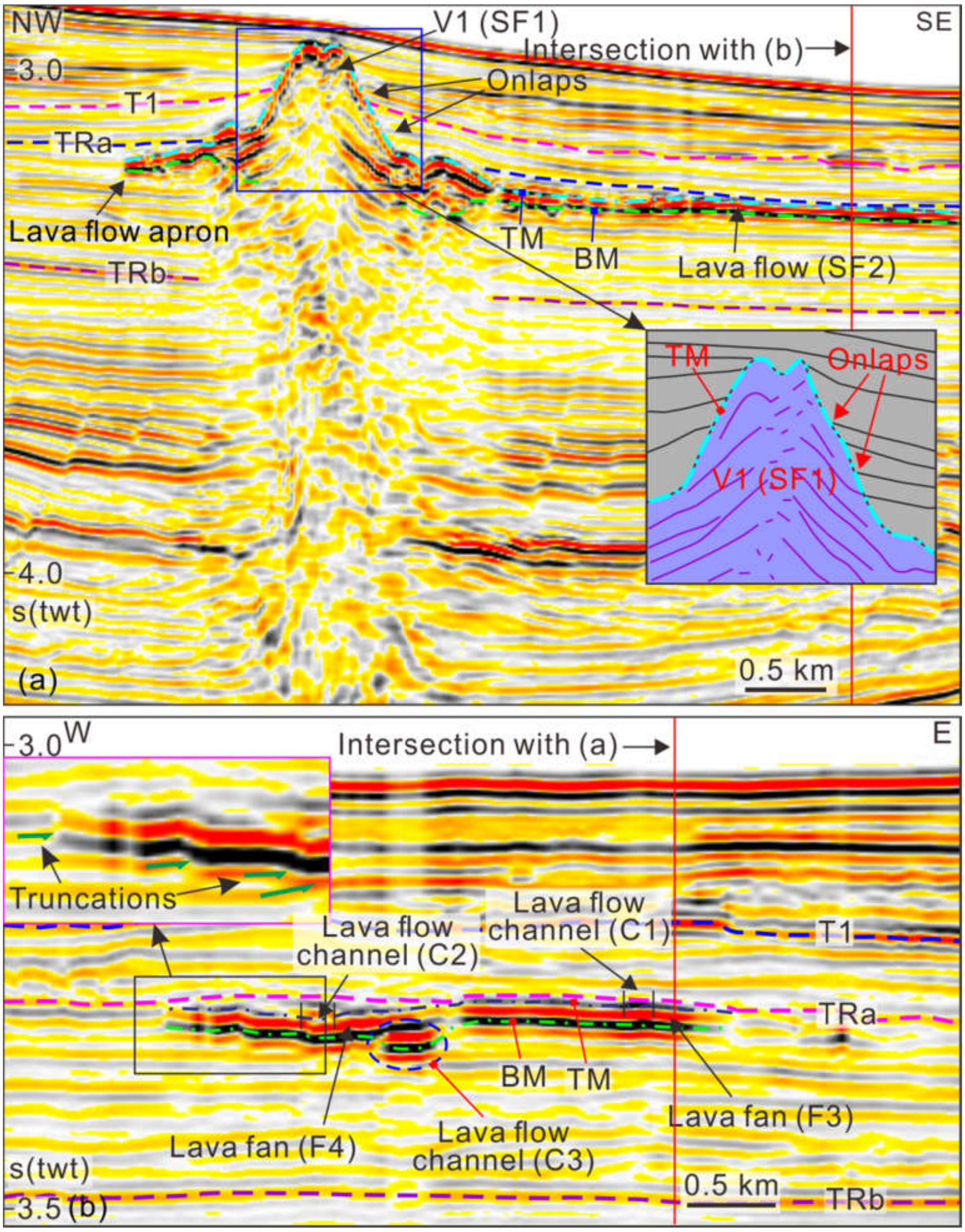

673

674 Figure 4

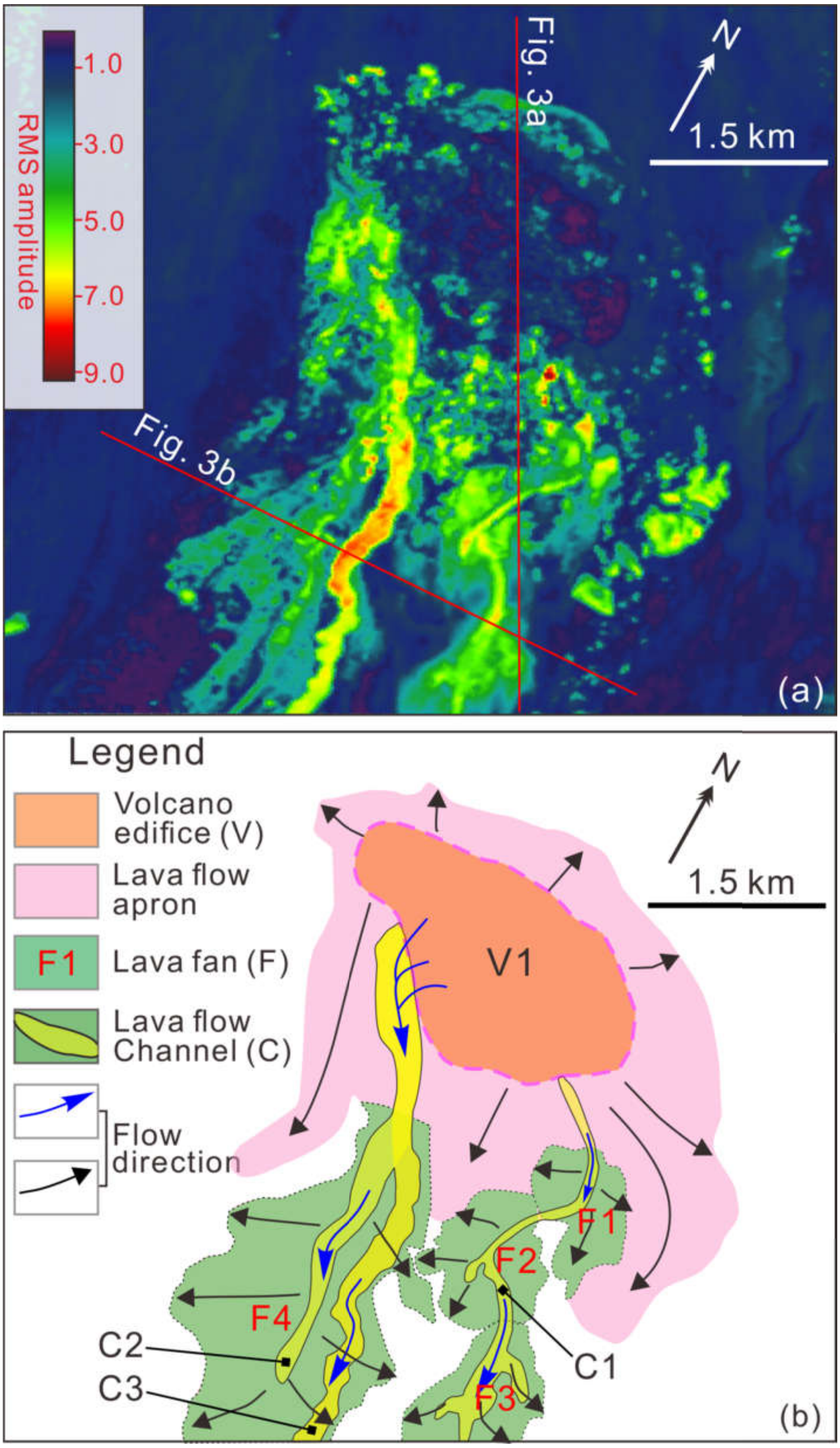

675

676 Figure 5

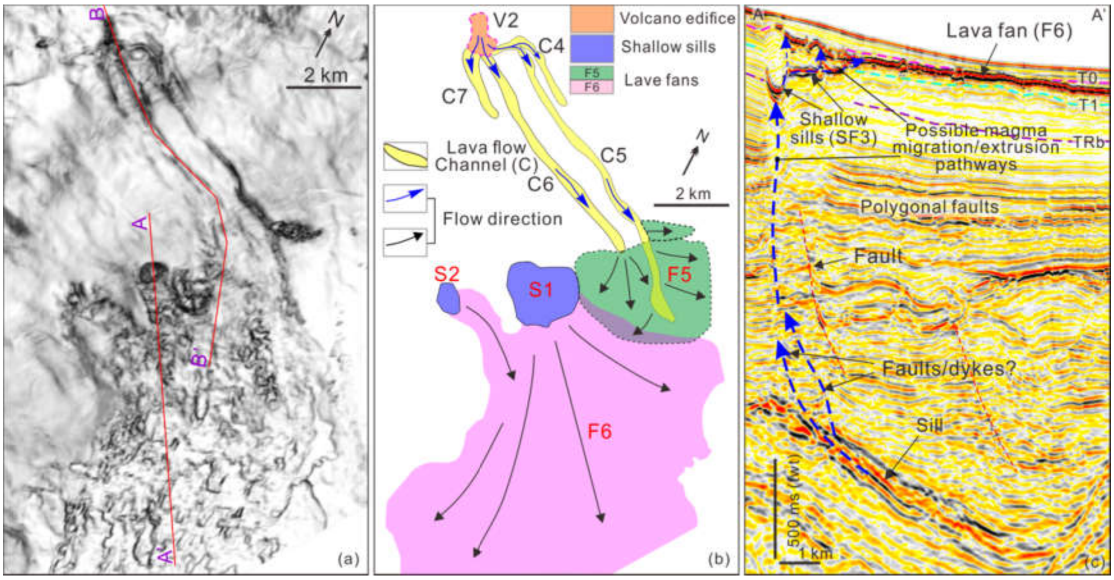

677

Figure 6

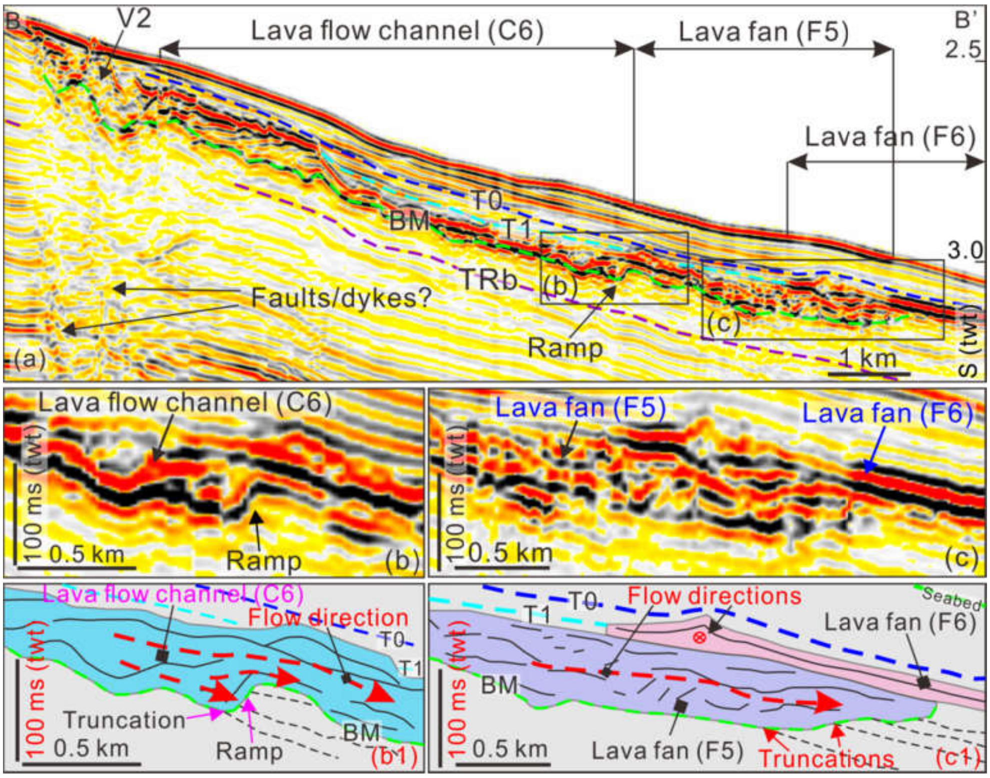

B
V2
Lava flow channel (C6)
Lava fan (F5)
B'
2.5
Lava fan (F6)
T0
BM
T1
TRb
(b)
(c)
Faults/dykes?
Ramp
3.0
1 km
S (twt)
(a)
Lava flow channel (C6)
100 ms (twt)
0.5 km
Ramp
(b)
Lava fan (F5)
Lava fan (F6)
100 ms (twt)
0.5 km
(c)
Lava flow channel (C6)
Flow direction
T0
T1
100 ms (twt)
Truncation
BM
0.5 km
Ramp
(b1)
T0
T1
Flow directions
Seabed
Lava fan (F6)
100 ms (twt)
BM
0.5 km
Lava fan (F5)
Truncations
(c1)